The 15th International Symposium on Magnetic Bearings, August 3-6, 2016, Mojiko Hotel, Kitakyushu, Japan

ISMB15

Experimental Verification of a Model-Based Zero- and Low-Speed Angle Observer for Bearingless Permanent Magnet Machines

Tobias WELLERDIECK*, Pascal REICHMUTH*, Daniel STEINERT** and Johann W. KOLAR*

* Power Electronic Systems Laboratory, ETH Zurich
Physikstrasse 3, 8092, Zurich, Switzerland

** Levitronix GmbH
Technoparkstrasse 1, 8005, Zurich, Switzerland

Abstract

Bearingless machines are used for a variety of applications with demand for low mechanical loss, low wear and low contamination. These machines use contact-free magnetic suspension to levitate the rotor. The control of the machine requires precise radial and angular position information in order to ensure stable levitation. This information is usually obtained with two types of sensors: radial displacement sensors and angle sensors. Alternatively, an angle-sensorless control scheme can be used, reducing the complexity and the cost of the machine. While such a control is well known for conventional machines it is challenging to adapt it for bearingless machines. The reason is that most methods fail to provide the angle information at zero- and low-speed but bearingless machines require knowledge about the rotor angle at all speeds in order to function.

The theoretical mode of operation of a model-based angle observer for zero- and low-speed operation of a bearingless machine was shown in previous publications. The observer obtains the rotor angle estimation error by analyzing the performance of the radial bearing and comparing it to the performance of a model with zero angle error. This observer can be used at zero- and at low-speeds.

This paper provides a more detailed description of the non-idealities of the zero- and low-speed observer and presents new results of machine operation without angle sensors. The generation of torque and force inside the machine is analyzed in more detail. The experimentally verified results of this paper indicate that the novel observer can be used up to speeds at which back-electromotive force estimation is possible.

Key words : Bearingless machine, angle observer, model based, sensorless, low-speed, zero-speed

1. Introduction

Bearingless machines are electric motors that combine the functions of an electric machine and a magnetic bearing in one stator, (Bichsel 1991), allowing for a compact machine design. The motor generates both the torque and the suspension forces required to levitate the rotor. This allows the elimination of a drive shaft and mechanical bearings and enables the rotor to be driven inside a sealed compartment, making bearingless machines well suited for applications with demands on high speed (Mitterhofer, Gruber, and Amrhein 2014), low wear and low particle generation (Neff, Barletta, and Schoeb 2002).

The rotor of the machine described in this paper consists of a ring shaped one pole-pair, radially-magnetized rare-earth magnet with a diameter that exceeds its height. This type of machine is called a heteropolar bearingless permanent magnet slice motor (Schoeb and Barletta 1995). The disk shape is chosen because it simplifies the control of the machine. Only the radial position and the rotor angle have to be actively controlled while axial movement and tilting around the radial axis are stable by design (Schoeb and Barletta 1997; Amemiya et al. 2005). Figure 1(b) depicts a render of the bearingless machine, showing the ring shape of the magnet, the stator iron and the windings that are used to produce the magnetic fields in the airgap. Parts of the mechanical structure and the case are not shown to make the ring shaped rotor and the stator structure visible.

The controller of the bearingless machine requires knowledge of both the radial and the angular rotor position in order to ensure stable levitation and high drive performance (Nussbaumer et al. 2011). The position is commonly obtained with

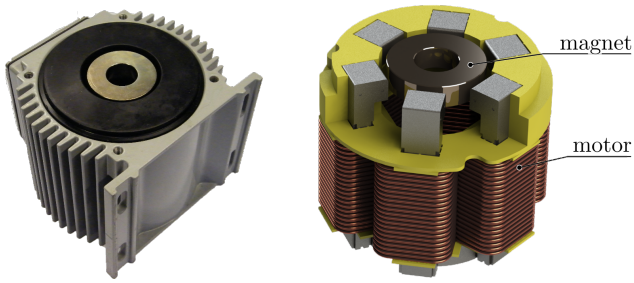

Fig. 1 The bearingless machine that is used to verify the control scheme (a) and a render of the machine showing the ring shaped rotor (b). Note that the rotor magnet is displaced in order to generate the displacement force required for the angle estimation.

the use of radial and angular sensor systems that are usually complex and sensitive to harsh environments. Omitting these sensors reduces the complexity and the cost. This can make bearingless machines suitable for applications in rough environments or applications with high cost sensitivity.

This paper focuses on the possibility to eliminate the angular position sensors. Multiple angle-sensorless rotor angle estimation techniques for permanent magnet synchronous machines have been reported in the literature (J.-S. Kim and Sul 1997; Acarnley and Watson 2006). These methods are of two types: the first type is based on the estimation of the back-electromotive force (EMF) (Park et al. 2001) and the second type uses high frequency (HF) signal injection (S. Kim and Ha 2008). The EMF-based control schemes work only above a minimum speed since they require sufficient amplitude of the induced voltage, which is proportional to the machine speed. Therefore, these methods are not suitable for zero- and low-speed operation. The HF signal injection methods rely on the fact that the machine inductances are dependent on the rotor angle due to saliency of the machine. While the method provides rotor angle information over the entire speed range of the machine it is limited to machines with salient pole rotors. Furthermore, the machine inductances in bearingless machines are also dependent on the radial rotor position. Therefore, a deviation in the radial position of the rotor will disturb the rotor angle estimation.

It is possible to use EMF based observers at in combination with a special low speed control method and drive the machine with a two stage controller. This approach is reported in literature by Raggl et al. (2009). The control scheme utilizes an open loop controller for zero- and low-speed operation. This paper proposes to replace the open-loop control with a closed-loop zero- and low-speed angle estimator. The zero- and low-speed angle estimator is model based, meaning that it utilizes a model of the bearing and compares the ideal model behavior with the actual bearing behavior. The novel observer allows to drive the machine up to the minimum speed at which EMF-based methods can take over.

The modelling of the magnetic flux around the rotor is shown in Section 2. The results of the flux modelling are used for the analysis of the torque and bearing force generation in the bearingless machine, which is presented in Section 3. Section 4 presents the functionality and the structure of the angle observer. The functionality of the observer is shown in Section 5 by measurements taken with the prototype machine shown in Fig. 1(a). Section 6 draws some conclusions, summarizes the results and gives some outlook on how the control scheme can be improved further.

2. Modelling of magnetic flux in around the rotor magnet

The torque and bearing force calculation is based on the analysis of the magnetic flux density in the airgap, similar to the analysis presented by Laptre et al. (2015). A FEM program was used to obtain the magnetic flux density around the rotor. Figure 2(a) and Fig. 2(b) show a schematic top and side view of the motor. The flux density analysis is done on the circles $\xi_{c1,\dots cn}$ on a cylindrical surface in the airgap and on $\xi_{t1,\dots,tm}, \xi_{b1,\dots,bl}$ on disks above and below the rotor. Note that the number of circles is reduced in the figures for the sake of clarity, the simulation is done for $n + m + l = 43$. The analysis of the flux density above and below the rotor is necessary since the short rotor has significant stray fields. The stray fields become larger if the rotor is displaced. The consideration of the stray fields is the most significant difference to the reduced analysis presented in (Wellerdieck, Nussbaumer, and Kolar 2016).

The flux density B around the rotor can be approximated by its space harmonics $B_{k,i}$ as

$$B_k(\alpha) \approx \sum_i \hat{B}_{k,i} \cos(i\alpha + \phi_{k,i}), k \in [(r,t,z),(x,y,z)] \quad (1)$$

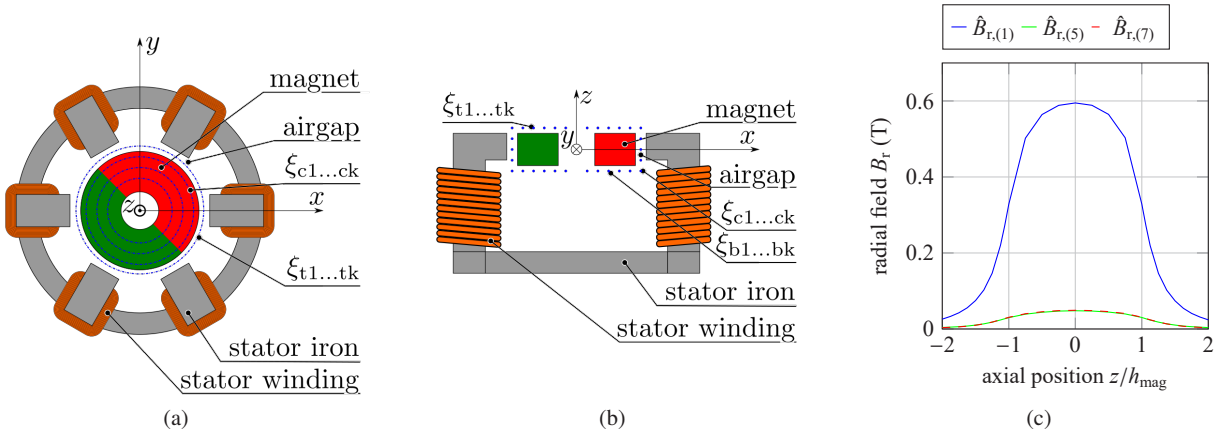

Fig. 2 Schematic top view (a) and side view (b) of the bearingless motor. The flux density is analyzed on the circles $\xi_{c1...ck}$ on a cylindrical surface around the rotor, $\xi_{t1,...tn}$ and $\xi_{b1,...bl}$ above and below the rotor. The amplitude of the radial component of the most prominent flux density harmonics in the arigap over axial position (c) showing that the flux is not constrained to the rotor height.

with $\hat{B}_{k,i}$, $\phi_{k,i}$ and α being the amplitude of the i-th harmonic, the phase of the harmonic and the angular position on one of the circles ξ. Equation (1) is used with cylindrical coordinates in the airgap and with cartesian coordinates on the top and bottom disks. Figure 2(c) shows the amplitude of the radial component of the fundamental, the fifth and seventh flux density harmonic for different axial positions in the airgap. This shows that the magnetic flux is not limited to the height of the rotor and an extension of the analysis to the top and bottom of the rotor is necessary.

Table 1 The variables that define the magnetic flux density around the rotor.

variable	description	range
Δx	displacement in x direction	$\Delta x \in [-2\,\text{mm}, 2\,\text{mm}]$
Δy	displacement in y direction	$\Delta x \in [-2\,\text{mm}, 2\,\text{mm}]$
θ	rotor angle	$\theta \in [0, 2\pi]$
$\hat{I}_D, \phi_D$	drive current amplitude and phase	$\hat{I}_D \in [0, 10\,\text{A}]\,, \phi_D \in [0, 2\pi]$
$\hat{I}_B, \phi_B$	bearing current amplitude and phase	$\hat{I}_B \in [0, 3\,\text{A}]\,, \phi_B \in [0, 2\pi]$

The magnetic fields around the rotor are dependent on the rotor position as well as the bearing and drive currents in the stator windings. If magnetic saturation is neglected, the amplitudes of the flux density harmonics can be calculated as a sum of four field components as

$$\hat{B}_{k,i} = \hat{B}_{k,i,0}(\theta) + \hat{B}_{k,i,\Delta}(\theta, \Delta x, \Delta y) + \hat{B}_{k,i,D}\left(\hat{I}_D, \phi_D\right) + \hat{B}_{k,i,B}\left(\hat{I}_D, \phi_B\right), k \in [(r,t,z),(x,y,z)] \tag{2}$$

and the phases can be stated as

$$\phi_{k,i} = \phi_{k,i,0}(\theta) + \phi_{k,i,\Delta}(\theta, \Delta x, \Delta y) + \phi_{k,i,D}(\phi_D) + \phi_{k,i,B}(\phi_B), k \in [(r,t,z),(x,y,z)]\,. \tag{3}$$

Table 1 lists the variables used in (2) and (3) and Tab. 2 shows how the relevant harmonics can be assigned to different field components in the airgap.

Table 2 The four field components and their relevant harmonics.

description	amplitude and phase	relevant harmonic number
zero displacement field	$\hat{B}_{k,i,0}, \phi_{k,i,0}$	$i \in [1, 5, 7, 11, 13]$
rotor displacement field	$\hat{B}_{k,i,\Delta}, \phi_{k,i,\Delta}$	$i \in [1 - 10]$
drive field	$\hat{B}_{k,i,D}, \phi_{k,i,D}$	$i \in [1, 5, 7, 11, 13]$
bearing field	$\hat{B}_{k,i,B}, \phi_{k,i,B}$	$i \in [2, 4, 8, 10, 12, 14, 16]$

The concept of the relevant harmonics can best be explained by example. Figure 3(a) and 3(c) show the radial and tangential field on the circle ξ_{c0} with the axial position $z = 0$, cf. Fig. 2(b). The middle position is chosen because the z component of the field is negligible due to symmetry. The bearing current is varied from 0 A to 3 A, while the rotor is at $\Delta x = \Delta y = 0\,\text{mm}$. Figure 3(b) and 3(d) show the amplitudes of the space harmonics $\hat{B}_{r,i}$ and $\hat{B}_{t,i}$. The constant amplitudes of the harmonics of the order 1, 5 and 7 of the zero displacement field are clearly visible. It can be seen that only the

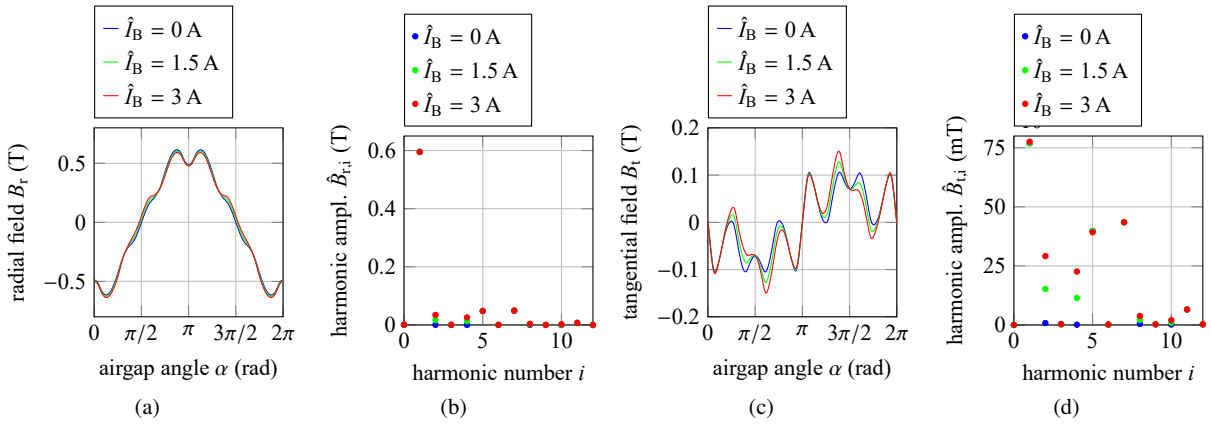

(a) (b) (c) (d)

Fig. 3 The field in the middle of the airgap at $z = 0$ mm for an undisplaced rotor and different bearing current amplitudes, with the radial field (a), the amplitudes of the radial space harmonics (b), the tangential field (c) and the amplitudes of the tangential space harmonics (d). Only a limited number of space harmonics are dependent on the bearing current.

harmonics of the order 2, 4, 8, 10 and 12 change with increasing bearing current while the other harmonics stay constant. The change of the amplitude is linear.

Only a small number of FEM simulations with different bearing current amplitudes are required to formulate a good model for the bearing field in the airgap. The same analysis can be done for the displacement and the drive field in the airgap and for the fields above and below the rotor. The advantage of this approach is that the field model, once it is formulated with the use of FEM simulations, can be evaluated computationally efficient. The model could even be implemented on the controller digital signal processor (DSP) to predict the bearing forces precisely.

3. Drive and bearing behavior

The torque and force acting on the rotor magnet can be calculated by evaluating the Maxwell stress tensor on a closed surface around the rotor. In this section, only magnetostatic forces are considered. The cylindrical surface is split into 43 parts and the magnetic flux density on each part of the surface is approximated by the most relevant space harmonics, cf. Section 2. Therefore, the surface integration becomes an integration on n cylinder parts on the circles $\xi_{c1,\dots cn}$,$\xi_{t1,\dots tn}$ and $\xi_{b1,\dots bl}$, cf. Fig. 2(a) and Fig.2(b). The torque and force due to the fields in the airgap can be calculated as

$$
\begin{aligned}
T_{z,c} &= \frac{R^2}{\mu_0} \sum_i^n H_i \int_0^{2\pi} B_{r,ci}(\alpha)\, B_{t,ci}(\alpha)\, d\alpha \\
F_{x,c} &= \frac{R}{2\mu_0} \sum_i^n H_i \int_0^{2\pi} \left(B_{r,ci}^2(\alpha) - B_{t,ci}^2(\alpha) - B_{z,ci}^2(\alpha)\right) \cos(\alpha) - 2B_{r,ci}(\alpha)\, B_{t,ci}(\alpha) \sin(\alpha)\, d\alpha \\
F_{y,c} &= \frac{R}{2\mu_0} \sum_i^n H_i \int_0^{2\pi} \left(B_{r,ci}^2(\alpha) - B_{t,ci}^2(\alpha) - B_{z,ci}^2(\alpha)\right) \sin(\alpha) + 2B_{r,ci}(\alpha)\, B_{t,ci}(\alpha) \cos(\alpha)\, d\alpha \\
F_{z,c} &= \frac{R}{\mu_0} \sum_i^n H_i \int_0^{2\pi} B_{r,ci}(\alpha)\, B_{z,ci}(\alpha)\, d\alpha
\end{aligned}
\tag{4}
$$

with $T_{z,c}$ being the torque in z direction and $F_{x,c}, F_{y,c}, F_{z,c}$ being the radial forces acting on the rotor. The radius of the circle $\xi_{c1,\dots cn}$ is denoted by R and the height of the i-th cylinder part is labeled H_i. The flux density components on the i-th cylinder part in radial, tangential and z-direction are labeled $B_{r,ci}$, $B_{t,ci}$ and $B_{z,ci}$, respectively. A similar torque and force calculation is done for the top and bottom parts of the enclosing surface.

Equation (4) in combination with the reduced harmonics approach allows for the precise calculation of the torque and bearing forces acting on the rotor. The calculation is computationally efficient since only additions and multiplications are required. However, the calculations become extensive if all the harmonics of Tab. 2 are used. Therefore, an example with a reduced number of harmonics is used to illustrate the behavior of the machine. The simplifications are: the z component of the field is neglected, the zero displacement field consists only of harmonics of the order 1 while the bearing and the displacement field consist only of harmonics of the order 2. It is assumed that the rotor is levitating at the position $x = x^* > 0, y = y^* = 0$ and $\theta = \hat{\theta} = 0$, with x, y denoting the rotor position, x^*, y^* denoting the reference rotor position

and $\theta, \hat{\theta}$ denoting the rotor angle and the estimated rotor angle, respectively. Figure 4(a) shows a schematic view of this mode of operation with $\vec{\Psi}_\mathrm{r}$, $\vec{F}_\Delta$ and $\vec{F}_\mathrm{B}$ denoting the flux direction of the permanent magnet, the force acting on the magnet due to the displacement and the bearing foce, respectively. The field in the airgap is

$$\begin{aligned}
B_{\mathrm{r},1}(\alpha) &= \hat{B}_{\mathrm{r},1,0}\cos(\alpha)\\
B_{\mathrm{t},1}(\alpha) &= \hat{B}_{\mathrm{r},1,0}\cos(\alpha-\pi/2)\\
B_{\mathrm{r},2}(\alpha) &= \hat{B}_{\mathrm{r},2,\Delta}\cos(2\alpha)+\hat{B}_{\mathrm{r},2,\mathrm{B}}\cos(2\alpha+\pi)\\
B_{\mathrm{t},2}(\alpha) &= \hat{B}_{\mathrm{r},2,\Delta}\cos(2\alpha-\pi/2)+\hat{B}_{\mathrm{r},2,\mathrm{B}}\cos(2\alpha+\pi/2)\,.
\end{aligned} \tag{5}$$

The field components are listed in Tab. 2. The amplitudes and harmonics fulfill

$$\begin{aligned}
\hat{B}_{\mathrm{r},2,\mathrm{B}} &= \hat{B}_{\mathrm{r},2,\Delta} \qquad \hat{B}_{\mathrm{t},2,\mathrm{B}} = \hat{B}_{\mathrm{t},2,\Delta}\\
\phi_{\mathrm{r},2,\mathrm{B}} &= \phi_{\mathrm{r},2,\Delta}+\pi \quad \phi_{\mathrm{t},2,\mathrm{B}} = \phi_{\mathrm{t},2,\Delta}+\pi.
\end{aligned} \tag{6}$$

The bearing controller of the machine has set the bearing current such that the net force acting on the rotor is

$$\vec{F} = \begin{bmatrix} F_\mathrm{x} \\ F_\mathrm{y} \end{bmatrix} = \vec{F}_\Delta - \vec{F}_\mathrm{B} = 0. \tag{7}$$

This is done by measuring the displacement x, y, calculating the bearing current $\vec{I}_\mathrm{B} = \begin{bmatrix} I_\mathrm{Bx} \\ I_\mathrm{By} \end{bmatrix}$ in the rotor coordinate system and then rotating the bearing current by $\hat{\theta}$ into the stator coordinate system.

The above is the normal, stable behavior of a bearing controller with correct rotor information. Now, it is assumed that the rotor angle θ is changed to $\theta > 0$ while the rotor angle estimation is kept at $\hat{\theta} = 0$, cf. Fig. 4(b). The bearing controller still applies the same bearing current since neither the position nor the angle estimation changed. The resulting flux density in the airgap is

$$\begin{aligned}
B_{\mathrm{r},1}(\alpha) &= \hat{B}_{\mathrm{r},1,0}\cos(\alpha-\theta)\\
B_{\mathrm{t},1}(\alpha) &= \hat{B}_{\mathrm{r},1,0}\cos(\alpha-\theta-\pi/2)\\
B_{\mathrm{r},2}(\alpha) &= \hat{B}_{\mathrm{r},2,\Delta}\cos(2\alpha-\theta)+\hat{B}_{\mathrm{r},2,\mathrm{B}}\cos(2\alpha+\pi)\\
B_{\mathrm{t},2}(\alpha) &= \hat{B}_{\mathrm{r},2,\Delta}\cos(2\alpha-\theta-\pi/2)+\hat{B}_{\mathrm{r},2,\mathrm{B}}\cos(2\alpha+\pi/2)\,.
\end{aligned} \tag{8}$$

Inserting (8) into (4) results a non-zero net force acting on the rotor. The reason is that the reference bearing force $\vec{F}^*_\mathrm{B}$ is not the same as the actual bearing force $\vec{F}_\mathrm{B}$. The rotor will move in y direction because the bearing current is not rotated by the correct rotor angle. This is an unstable mode of operation. The bearing force acting on the rotor can be expressed in terms of $\vec{F}^*_\mathrm{B}$ and the angle estimation error $\Delta\theta = \hat{\theta} - \theta$ as

$$\vec{F}_\mathrm{B} = \begin{bmatrix} \cos(\Delta\theta) & -\sin(\Delta\theta) \\ \sin(\Delta\theta) & \cos(\Delta\theta) \end{bmatrix} \vec{F}^*_\mathrm{B}. \tag{9}$$

The movement in y direction will be detected by the y-direction position controller. The y-axis bearing controller will adjust for this movement and reduce I_By. Figure 4(c) shows the effect of this. The reference bearing force has been turned by the two bearing controllers until $\vec{F}_\mathrm{B} = \vec{F}_\Delta$ is fulfilled and the rotor is stable again.

Equation (9) describes an approximation of the actual coupling. It is correct for the simple example with only first and second order harmonics. Figure 5(a) shows the forces acting on a displaced rotor with the rotor angle being changed from 0 to 2π while the estimated angle is kept $\hat{\theta} = 0$. The forces calculated with all the harmonics shown in Tab. 2 are labeled $F_\mathrm{x,c}, F_\mathrm{y,c}$ and the forces calculated with the simplified approach are denoted $F_\mathrm{x,s}, F_\mathrm{y,s}$. This shows that (9) really is only a rough estimation. However, Section 5 shows that the estimation is sufficient to control the machine.

This section shows how an error in the rotor position results in a coupling of the bearing control in x and y direction. This coupling effect is used to calculate the rotor angle estimation error and to update the rotor angle estimate. The method works only for sufficiently small estimation errors since the radial position controllers fail to stabilize the rotor if the coupling is too strong.

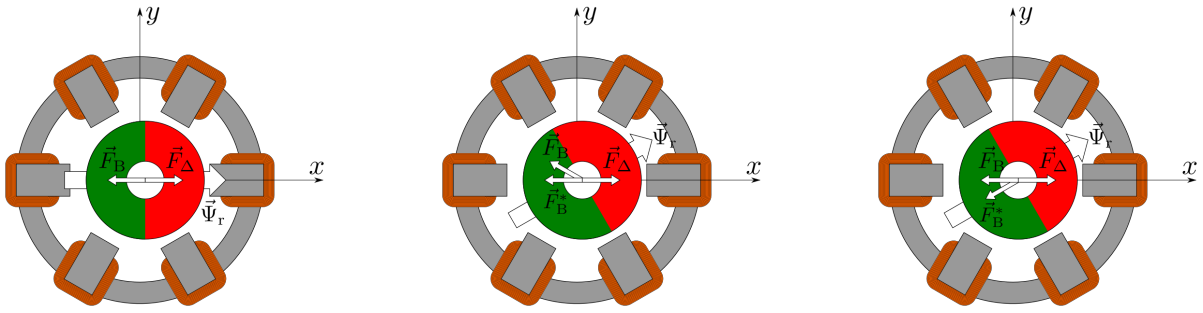

(a) (b) (c)

Fig. 4 Schematic top view of the bearingless machine showing an operating point with zero rotor angle estimation error (a), operation point with non-zero angle estimation error without the compensation of the bearing controllers (b) and with the compensation (c).

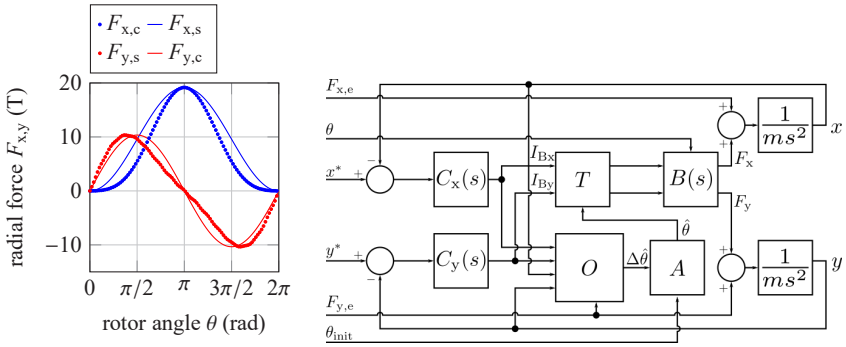

(a) (b)

Fig. 5 Radial forces acting on a displaced rotor if the rotor is rotated but the rotor angle estimate is not updated (a) and simplified controller block diagram of the bearingless machine neglecting the current controllers and the speed control (b).

4. Observer structure

The angle observer utilizes the force coupling described in (9) to estimate the rotor angle estimation error and the fact that the two bearing controllers will compensate the coupling for small angle estimation errors.

Figure 5(b) shows a schematic controller block diagram of the bearingless machine. The speed control is not shown and the sensors are modelled to work without measurement error. Furthermore, the current controllers are assumed to work perfectly and, therefore, are not shown. Note, that s is the Laplace operator and m is the rotor mass. The two radial position controllers are labeled $C_x(s)$ and $C_y(s)$ and are of a PID structure. The bearing controllers calculate the bearing current reference in the rotor oriented coordinate system I_{Bx} and I_{By} based on the difference between the rotor position x^* and y^* and the rotor reference positon x, y. The bearing currents are then rotated into the stator coordinate system in the block T. $B(s)$ denotes the force generation in the machine. Double integrating the sum of the internal forces F_x and F_y and any external radial forces acting on the rotor $F_{x,e}$ and $F_{y,e}$ yield the rotor position. The rotor angle estimation observer is labeled O an the angle estimation update function is labeled A.

The observer block O calculates an estimate of the rotor angle error as

$$\Delta\theta = \angle\left(\vec{F}_B^*\right) - \angle\left(\vec{F}_{r,e}\right) - 2\pi = \angle\left(\vec{I}_B\right) - \angle\left(\vec{F}_{r,e}\right) - 2\pi. \tag{10}$$

The bearing current angle is known since the bearing currents are defined by the radial position controllers. The external radial force $F_{r,e}$ consists of three parts:

$$\vec{F}_{r,e} = \vec{F}_\Delta + \vec{F}_g + \vec{F}_\delta \tag{11}$$

with $\vec{F}_\Delta$, $\vec{F}_g$ and $\vec{F}_\delta$ being the force due to radial displacement of the rotor, the radial gravitational pull and any disturbance

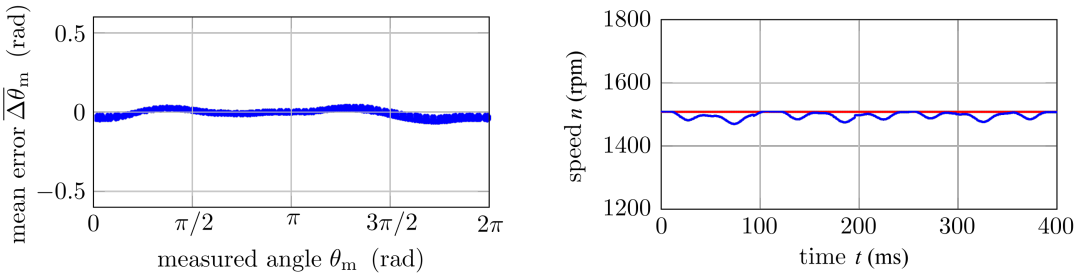

Fig. 6 Mean rotor angle estimation error during operation of the bearingless machine prototype with constant speed of 1500 rpm (a), actual and reference speed during operation (b).

forces, respectively. The angle of the displacement force is

$$\angle\left(\vec{F}_\Delta\right) = \angle\left(\vec{r}\right) \tag{12}$$

with $\vec{r}$ being the radial displacement. Therefore, the angle of the displacement force can be calculated based on the measurements of the radial rotor position x, y. The radial gravitational pull is dependent on the orientation of the machine. Its direction can be measured after the start-up by checking the bearing currents if the rotor is levitating at $x^*, y^* = 0$. The rotor is displaced if no radial gravitational pull is detected in order to generate a known $\vec{F}_\mathrm{r,e}$. The unknown disturbance forces are usually application dependent or arise from rotor imbalances. However, application dependent disturbances are usually speed dependent, such as hydraulic forces in fans or pumps, and so are inbalance forces. Nevertheless, any disturbance force will lead to an undetectable angle estimation error $\Delta\theta_\delta$. The biggest undetectable estimation error $\Delta\hat{\theta}_\delta$ occurs if the disturbance force is perpendicular to the known radial forces and can be calculated as

$$\Delta\hat{\theta}_\delta = \arctan\left(\frac{|\vec{F}_\delta|}{|\vec{F}_\Delta + \vec{F}_\mathrm{g}|}\right). \tag{13}$$

The observer presented in this paper is able to detect the rotor angle estimation error. Subsequently, the angle estimation is calculated by updating the angle estimation with

$$\hat{\theta}(t) = \hat{\theta}_\mathrm{init} + P \cdot \Delta\theta(t) + I \cdot \int_0^t \Delta\theta(\tau)\, d\tau \tag{14}$$

with P, I being the proportional and integrator gain of the update function A and $\hat{\theta}_\mathrm{init}$ being the initial rotor angle. The initial angle estimation is possible if the rotor is not levitating by evaluating the radial position sensors as shown by Raggl et al. (2009).

5. Verification

The verification is done with the bearingless machine shown in Fig. 1(a). The machine is operated in a no-load condition. The control of the machine is executed on a DSP. The DSP communicates with a computer and allows to display register values directly. The machine was placed with the gravity pulling in z direction of the rotor. Therefore, the known part of the external radial force $\vec{F}_\mathrm{r,e}$ is generated by setting the rotor reference position to $x^* = 0.5\,\mathrm{mm}$, $y^* = 0.5\,\mathrm{mm}$.

The machine is fitted with rotor angle sensors to measure the rotor angle θ_m. The measured rotor angle is not used for the control of the machine. Figure 6(a) shows the mean of the difference between estimated and observed rotor angle $\overline{\Delta\theta}_\mathrm{m} = \hat{\theta} - \theta_\mathrm{m}$ for multiple rotations. Note that $\Delta\theta \neq \Delta\theta_\mathrm{m}$ since the observer performance is degraded by parasitic effects and disturbance forces. The estimator performance is sufficient to ensure stable levitation. Figure 6(b) shows the reference rotor speed n^* and the estimated speed $\hat{n}$. The speed estimate is calculated as

$$n^* = \frac{\partial\hat{\theta}}{\partial t} \cdot \frac{60}{2\pi} \cdot \frac{\mathrm{rpm}}{\mathrm{s}}. \tag{15}$$

The verification shows that the angle observer is able to estimate the rotor angle with sufficient accuracy for speeds up to 1500 rpm which is 15 % of the nominal machine speed. It is possible to switch the angle estimation to a back-EMF based scheme and then drive the machine up to the maximum speed.

6. Conclusion

The angle observer structure shown in this paper allows for the detection of the rotor angle at zero- and low machine speeds in bearingless machines. The observer is based on the fact that a rotor angle estimation error leads to a coupling of the radial position control in x and y direction. This coupling can be measured by evaluating the bearing currents. The observer uses an initial rotor angle estimation and updates it continuously. The method is based on the assumption that the radial disturbance forces acting on the rotor are small. The validity of this assumption is depending on the application of the bearingless machine and the maximum speed at which the observer is used.

The functionality of the method is shown by measurements with a prototype. A machine speed of 1500 rpm can be reached. This corresponds to 15 % of the nominal speed. A back-EMF observer can be used for the angle estimation at higher machine speeds.

The quality of the angle estimation can be improved if the coupling matrix, cf. (9), is adapted to represent the effect of all the harmonics. This would then allow to also adapt the angle estimation function shown in (10).

7. Acknowledgement

This work was supported by the *Swiss Commission for Technology and Innovation CTI-KTI*.

References

Acarnley, P.P. and Watson, J.F. (2006). "Review of position-sensorless operation of brushless permanent-magnet machines". In: *Industrial Electronics, IEEE Transactions on* 53.2, pp. 352–362.

Amemiya, J. et al. (2005). "Basic characteristics of a consequent-pole-type bearingless motor". In: *Magnetics, IEEE Transactions on* 41.1, pp. 82–89.

Bichsel, J. (1991). "The Bearingless Electrical Machine". In: *Proc. 1th Int. Symp. Magnetic Suspension Technology*, pp. 561–573.

Kim, Joohn-Sheok and Sul, Seung-Ki (1997). "New approach for high-performance PMSM drives without rotational position sensors". In: *Power Electronics, IEEE Transactions on* 12.5, pp. 904–911.

Kim, Sung-Yeol and Ha, In-Joong (2008). "A New Observer Design Method for HF Signal Injection Sensorless Control of IPMSMs". In: *Industrial Electronics, IEEE Transactions on* 55.6, pp. 2525–2529.

Laptre, B. et al. (2015). "New Model of Radial Force Determination in Bearingless Motor". In: *IEEE Transactions on Magnetics* 51.3, pp. 1–4.

Mitterhofer, H., Gruber, W., and Amrhein, W. (2014). "On the High Speed Capacity of Bearingless Drives". In: *IEEE Transactions on Industrial Electronics* 61.6, pp. 3119–3126.

Neff, M., Barletta, N., and Schoeb, R. (2002). "Bearingless centrifugal pump for highly pure chemicals". In: *Proc. 8th ISMB*, pp. 283–287.

Nussbaumer, T. et al. (2011). "Magnetically Levitated Slice Motors - An Overview". In: *Industry Applications, IEEE Transactions on* 47.2, pp. 754–766.

Park, Han-Woong et al. (2001). "Position sensorless speed control scheme for permanent magnet synchronous motor drives". In: *Industrial Electronics, 2001. Proceedings. ISIE 2001. IEEE International Symposium on*. Vol. 1, 632–636 vol.1.

Raggl, K. et al. (2009). "Robust Angle-Sensorless Control of a PMSM Bearingless Pump". In: *Industrial Electronics, IEEE Transactions on* 56.6, pp. 2076–2085.

Schoeb, R. and Barletta, N. (1995). "Principle and Application of a Bearingless Slice Motor". In: *Proc. 5th Int. Symp. Magnetic Bearings*, pp. 313–318.

Schoeb, R. and Barletta, N. (1997). "Magnetic Bearing. Principle and Application of a Bearingless Slice Motor." In: *JSME International Journal Series C Mechanical Systems, Machine Elements and Manufacturing* 40.4, pp. 593–598.

Wellerdieck, T., Nussbaumer, T., and Kolar, J. (2016). "Angle-Sensorless Zero- and Low-Speed Control of Bearingless Machines". In: *IEEE Transactions on Magnetics* PP.99, pp. 1–1.